Topology-optimized phoxonic crystals with simultaneous acoustic and photonic helical edge states

Yafeng Chen,[1] Shuowei An,[1] Zhihao Lan,[2,*] Liang An,[1,†] and Zhongqing Su[1,‡]
[1]*Department of Mechanical Engineering, The Hong Kong Polytechnic University, Hong Kong SAR, People's Republic of China*
[2]*Department of Electronic and Electrical Engineering, University College London, London WC1E 7JE, United Kingdom*

(Received 4 May 2024; accepted 30 October 2024; published 19 November 2024)

Sonic and photonic topological insulators that host topological edge states offer promising potentials for the resilient control of acoustic and electromagnetic waves, respectively. Despite the great progress on sonic or photonic topological insulators, the research of their integration, i.e., the phoxonic topological insulator, is less explored. In this work, we propose a phoxonic topological insulator that hosts acoustic and dual-polarization photonic helical edge states simultaneously. In specific, we first design a glide-symmetric phoxonic crystal with concurrent sonic and dual-polarization photonic bandgaps via the topology optimization method. Then by choosing two different unit cells from the optimized phoxonic crystal and assembling them to create a domain-wall interface, a phoxonic topological insulator that supports two pairs of gapless helical edge states within both the sonic and photonic bandgaps is constructed. Pseudospin-locked unidirectional transmissions and robust manipulations of helical edge states are demonstrated for acoustic and dual-polarization electromagnetic waves simultaneously in the proposed phoxonic topological insulator. The designed phoxonic topological insulator opens new avenues for developing topological photoacoustic devices, enabling the reliable management of both acoustic and electromagnetic waves, as well as the investigation of their interplay.

DOI: 10.1103/PhysRevResearch.6.043166

I. INTRODUCTION

The discovery of topological insulators (TIs), which host topologically protected edge states that are immune to impurities and defects, has opened a new chapter in condensed state physics [1,2]. As the key concepts of topology are based on band theory, which also applies to classical wave systems, TIs have been extended to photonic and sonic crystals. Inspired by TIs in electronic systems, a kaleidoscopic range of photonic and sonic TIs have been developed [3–9]. The initial versions of photonic and sonic TIs are realized by incorporating either external magnetic fields or circulating fluids to break the time-reversal symmetry, thereby emulating the well-known quantum Hall effect [10–14]. However, the complexity to implement time-reversal symmetry breaking components makes these systems incompatible with integrated photonic and acoustic devices. In order to tackle this limitation, photonic and sonic TIs made of purely passive structures, which fully utilize the crystalline symmetry, have been developed. For example, by breaking the spatial symmetry of C_3-symmetric lattices to lift the degeneracy at the Dirac points, photonic and sonic TIs that host valley kink states have been constructed [15–18]. Meanwhile, by expanding and shrinking C_{6v}-symmetric lattices to gap out the double Dirac cone to open trivial and nontrivial bandgaps, photonic and sonic TIs that host pseudospin-dependent helical edge states have been achieved [19–23]. In addition, nonsymmorphic symmetry, which includes glide and screw symmetries, has also been demonstrated as an effective method to create sonic and photonic TIs that feature helical edge states [24–26]. Moreover, by engineering crystalline structures with distinct topological indexes, higher-order photonic and sonic TIs that host multidimensional edge and corner states have been further proposed [27–32].

Despite the fruitful achievements in photonic and sonic TIs, the research on their integration into phoxonic TIs (PTIs), which can be used for manipulating both electromagnetic and acoustic waves as well as their interaction, remains nascent. For example, Xia *et al.* designed a PTI in honeycomb lattice that simultaneously exhibits the topologically protected edge propagation of sound and light [33] whereas Hu *et al.* created a PTI with topological pseudospin-dependent edge states for both sound and light in honeycomb lattice with triangular rods [34]. However, these works are achieved based on hexagonal lattices, having limitations in engineering 90-degree sharp bend topological waveguides. Moreover, the pseudospin-dependent edge states hosted by these systems only form one single pair and are all gapped, limiting their robustness and multiband communication applications.

As crystalline symmetry crucially determines the physical mechanism and performance of PTIs, it is highly desirable to explore PTIs in other symmetric lattices. In this work, we design a PTI made of topology-optimized phoxonic crystals with glide symmetry in square lattice, which exhibits a number of

*Contact author: lanzhihao7@gmail.com
†Contact author: liang.an@polyu.edu.hk
‡Contact author: zhongqing.su@polyu.edu.hk

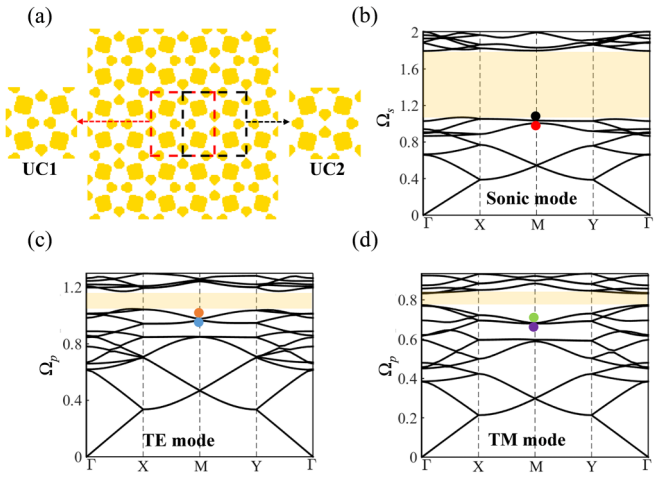

FIG. 1. (a) The designed PTI based on topology-optimized phoxonic crystal made of all-dielectric materials of silicon (yellow regions) in air. Two unit cells (UC1 and UC2) with different topological properties are selected from the phoxonic crystal for constructing waveguiding domain-wall interfaces. [(b)–(d)] The band structures of the phoxonic crystal for the (b) sonic, (c) TE, and (d) TM modes, respectively. The colorful circles mark the two pairs of degenerate bands at the *M* point below the bandgaps, whose eigenmode profiles are used to demonstrate the distinct topological properties between UC1 and UC2.

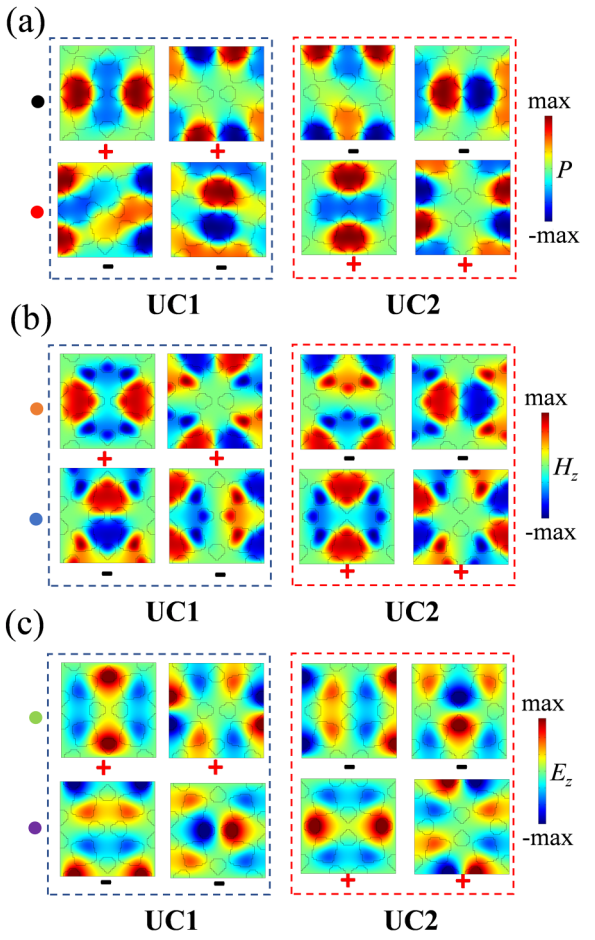

FIG. 2. Parities of the eigenmode profiles at *M* point of the two pairs of degenerate bands below the bandgap [marked by the colorful circles in Figs. 1(b)–1(d)] for UC1 and UC2 corresponding to the (a) sonic modes, (b) TE modes, and (c) TM modes, respectively, which show that for both pairs of degenerate bands and for all the sonic, TE, and TM modes, the two unit cells always possess opposite parities, a crucial condition for the design of the PTI.

features not present in previous works. In particular, our designed PTI supports two pairs of gapless helical edge states for sonic, transverse electric (TE) and transverse magnetic (TM) modes simultaneously. Pseudospin dependent one-way propagations are achieved for both acoustic and dual-polarization electromagnetic waves. Robust transmissions of edge states passing through a 90-degree sharp bend channel for both sonic and photonic modes are successfully demonstrated. Moreover, experimental results to validate the topological sonic edge modes are also provided. Our work suggests a new route for engineering PTIs, which have promising potential for applications in constructing topological photoacoustic devices.

II. RESULTS AND DISCUSSIONS

Due to the nontrivial nature of designing a phoxonic crystal with simultaneous sonic, TE and TM bandgaps, we employ the inverse design method based on topology optimization, which has been shown to be advantageous for designing both topological photonic and phononic crystals [35]. The materials of the phoxonic crystal are considered to be made of silicon and air for manipulating acoustic and electromagnetic waves simultaneously. For controlling the electromagnetic waves, silicon with permittivity of $\epsilon = 12$ is chosen, which can be taken as sound hard boundary for steering acoustic waves. As crystalline symmetry crucially determines the topological properties of sonic and photonic TIs, in this work, we constrain the unit cell (UC) with glide and mirror symmetries, which play a key role in realizing sonic and photonic TIs for hosting helical edge states [24,36], and then use the inverse design method (for details, see the Appendix) to open sonic and dual-polarization bandgaps simultaneously. The optimized phoxonic crystal and its band structures for the sonic, TE and TM modes are presented in Fig. 1(a) and Figs. 1(b)–1(d), respectively. From the band structures shown in Figs. 1(b)–1(d), one can see that the designed phoxonic crystal hosts bandgaps for both the acoustic and electromagnetic waves, i.e., the 8^{th}-order bandgap for the sonic modes, and the 12^{th}-order bandgap for the TE and TM modes. For the sake of simplicity, we normalize the frequency of sonic mode and photonic mode as $\Omega_s = \omega a/2\pi c_a$ and $\Omega_p = \omega a/2\pi c_{EM}$, respectively, where a denotes the lattice constant, c_a the velocity of acoustic waves in air and c_{EM} the velocity of EM waves in vacuum, respectively. The normalized frequency window of the bandgap for the sonic, TE, and TM modes is (1.0706, 1.7969), (1.0482, 1.1707), and (0.7739, 0.8325), respectively.

To construct waveguiding domain-wall interfaces, we select two different UCs from the designed phoxonic crystal: the primitive UC (UC1) and another UC (UC2) obtained by horizontally shifting UC1 by a/2 [see Fig. 1(a)], which is a common way to select unit cells with distinct topological properties [37]. We would like to note that though UC1 and UC2 are chosen from the same phoxonic crystal and thus

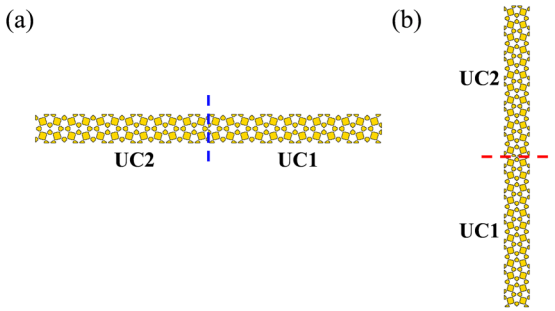

FIG. 3. Schematic of the supercell with (a) vertical and (b) horizontal interface between two domains made of UC1s and UC2s for studying the emergent topological edge states along the domain-wall interface.

exhibit identical band diagrams, their eigenmode profiles at high symmetry points may differ, which can lead to distinct topological properties between them. Importantly, from the band structures presented in Figs. 1(b)–1(d), one can observe that the imposed glide symmetry on the designed phoxonic crystal leads to a double degeneracy of all the bands along the MX boundary line of the Brillouin zone.

Figures 2(a)–2(c) show the parity distributions of the eigenmode profiles at M point of the two pairs of degenerate bands below the bandgap [labeled by the colorful circles in Figs. 1(b)–1(d)] for the two unit cells corresponding to the sonic, TE, and TM modes, respectively. Note that while monopolar and quadrupolar modes have a positive parity, dipolar modes have a negative parity and as such, it can be seen that the two unit cells always possess opposite parities for each pair of degenerate bands for all the sonic, TE, and TM modes, which are crucial for the design of PTIs. According to the Jackiw-Rebbi theory [38], if a domain-wall interface is created between two domains constructed using UC1 and UC2, topological edge states will emerge within the bandgap due to the different parities of UC1 and UC2. An interesting feature of our designed phoxonic crystal is that as there are two pairs of degenerate bands with parity-inversions below the bandgaps, two pairs of topological helical edge states in principle should emerge within the corresponding bandgaps, which will be demonstrated below.

To verify the emergence of topological edge states along a domain-wall interface between two domains made of UC1s and UC2s, we build two supercells consisting of 6 UC1s and 6 UC2s, separated by a vertical and horizontal interface, respectively [see Figs. 3(a) and 3(b)]. Note that as the UCs of the phoxonic crystal do not have C_4 symmetry, it is necessary to distinguish two different interfaces along the vertical and horizontal directions.

The band structures of the supercell for the sonic, TE, and TM modes with vertical and horizontal interface, are presented in Figs. 4(a)–4(c) and Figs. 4(d)–4(f), respectively. From the figures, we can see that for all the sonic, TE, and TM modes, two pairs of helical edge states with each pair consisting of two bands with opposite group velocities intersecting at $k_{y(x)} = \pi/a$ emerge within the corresponding bandgap. The degeneracy of the helical edge states at $k_{y(x)} = \pi/a$ arises from the synergy between the space group symmetry of the supercell and its periodicity along the glide

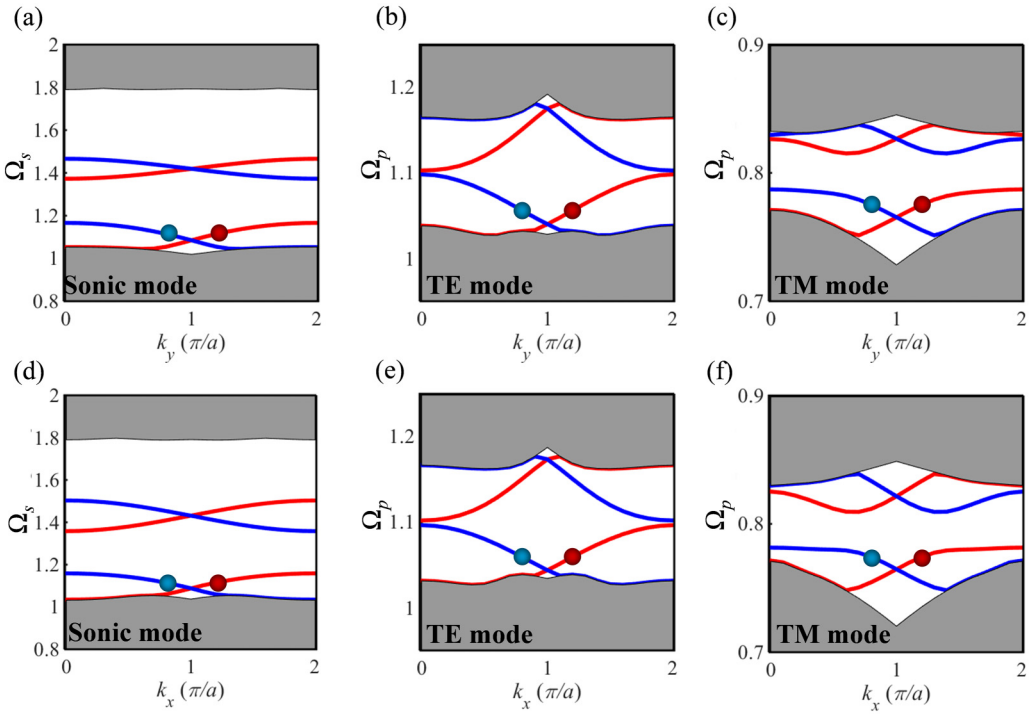

FIG. 4. [(a)–(c)] Band structures of the supercell with vertical interface for the (a) sonic, (b) TE, and (c) TM modes, respectively. [(d)–(f)] Band structures of the supercell with horizontal interface for the (f) sonic, (e) TE, and (f) TM modes, respectively. Each bandgap hosts two pairs of gapless helical edge states (blue and red) whereas the grey regions indicate the bulk states. Two edge states at k_y or $k_x = 0.9\pi/a, 1.1\pi/a$ are marked by the colored dots whose mode properties are presented in Fig. 5.

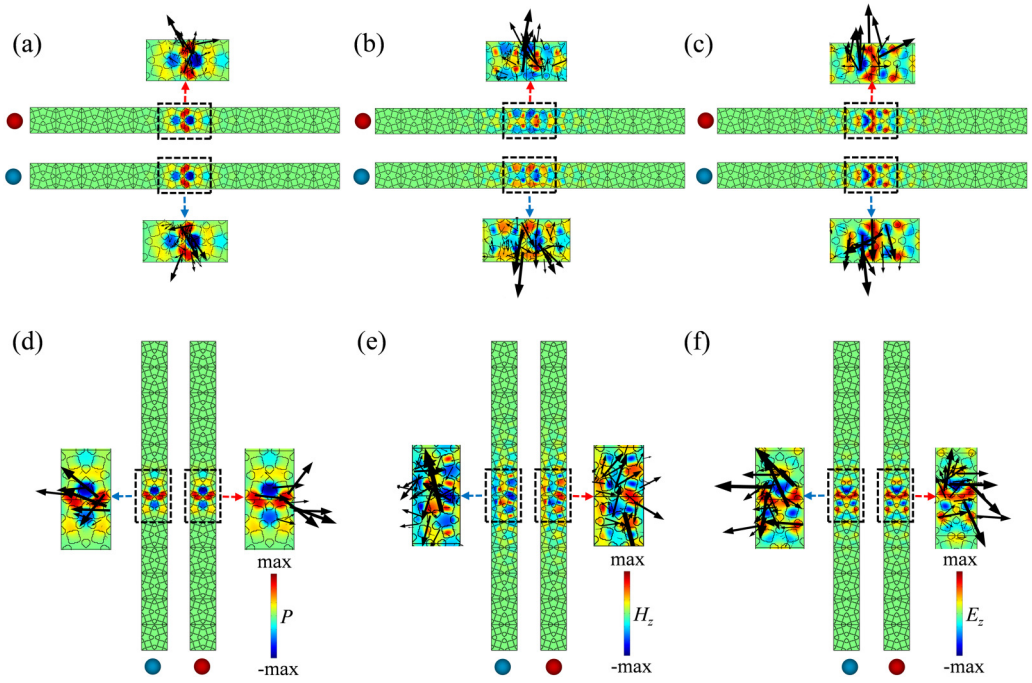

FIG. 5. [(a)–(c)] Eigenmode profiles and energy flux distributions for the edge states marked by the colored dots in Figs. 4(a)–4(c) hosted by the vertical interface for the (a) sonic modes, (b) TE modes, and (c) TM modes, respectively. [(d)–(f)] Eigenmode profiles and energy flux distributions for the edge states marked by the colored dots in Figs. 4(d)–4(f) hosted by the horizontal interface for the (d) sonic modes, (e) TE modes, and (f) TM modes, respectively.

dislocation [24,36]. For the vertical interface, the frequency windows of the two pairs of helical edge states for the sonic modes are (1.0445, 1.1662) and (1.3726,1.4660) whereas they are (1,0383, 1.0982) and (1.1028, 1.1625) for the TE modes, as well as (0.7711, 0.7871) and (0.8152, 0.8265) for the TM modes. On the other hand, for the horizontal interface, the frequency windows of the two pairs of helical edge states for the sonic modes are (1.0349, 1.1586) and (1.3583,1.5032) whereas they are (1,0315, 1.0964) and (1.1019, 1.1624) for the TE modes as well as (0.7714, 0.7815) and (0.8094, 0.8252) for the TM modes. Note that though the two interfaces are different, the emergent helical edge states within the corresponding bandgaps show similar features. Moreover, some parts of the bands of the helical edge states are imbedded within the bulk states (grey regions) due to the fact that the sizes of the bandgaps are not large enough. Most importantly, compared with previous PTIs that host gapped helical edge states [33,34] because of the broken C_{6v} symmetry at the domain-wall interface, the helical edge states in our designed PTI are all gapless, which is crucial for the robustness to steer acoustic and electromagnetic waves.

The eigenmode profiles and corresponding energy flux distributions for the first pair of edge states marked by the colored dots in Fig. 4 are presented in Fig. 5, from which one can see that the fields are mainly distributed around both the vertical and horizontal interfaces for all the sonic, TE and TM modes, demonstrating their edge states nature. Furthermore, from the energy flux distributions, we can observe that, for all the sonic, TE and TM modes, the energies of the edge states hosted by the vertical (horizontal) interface at $k_y(k_x) = 0.9\pi/a$ and $k_y(k_x) = 1.1\pi/a$ flow downward (leftward) and upward (rightward), respectively. This special feature indicates that these edge states possess chirality associated with finite orbital angular momentum (OAM), which could be exploited for pseudospin-locked one-way propagations.

To demonstrate that the helical edge states in the designed PTI for all the sonic, TE and TM modes exhibit pseudospin-locked unidirectional transmissions that are robust against sharp bends, we construct two waveguide structures with a straight and a bend channel as shown in Figs. 6(a) and 6(b), respectively. First, to demonstrate the pseudospin-locked unidirectional transmissions for all the sonic, TE and TM modes, a chiral source consisting of four antennas is placed at the middle of the straight interface in Fig. 6(a) for launching acoustic or electromagnetic waves. By configuring the phase winding of the four antennas, the chiral source can excite a wave either with positive OAM characterized by a counterclockwise

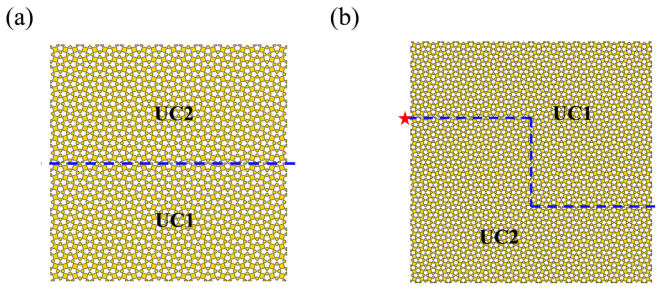

FIG. 6. Schematic waveguide structure with (a) straight and (b) bend channel between two domains made of UC1s and UC2s for studying pseudospin-locked unidirectional transmissions of the helical edge states and robustness of the transmissions against sharp bends.

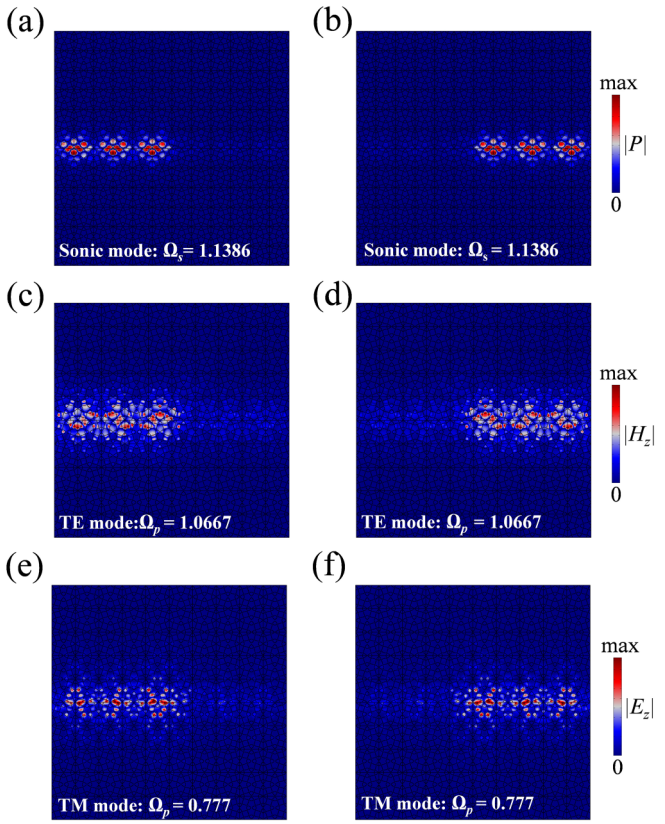

FIG. 7. Pseudospin-locked unidirectional transmissions of the sonic, TE and TM modes. [(a), (b)] Leftward and rightward one-way transmissions of acoustic waves possessing (a) negative and (b) positive OAM, respectively. [(c), (d)] Leftward and rightward one-way transmissions of the TE electromagnetic waves carrying (c) negative and (d) positive OAM, respectively. [(e), (f)] Leftward and rightward one-way transmissions of the TM electromagnetic waves carrying (e) negative and (f) positive OAM, respectively.

energy flow, or negative OAM with a clockwise energy flow. Figure 7 shows the field distributions of the excited sonic and electromagnetic waves when the source has a positive or negative OAM, demonstrating that waves of sonic, TE and TM modes that carry negative OAM propagate leftward unidirectionally [as shown in Figs. 7(a), 7(c) and 7(e)], whereas those carrying positive OAM propagate rightward unidirectionally [as shown in Figs. 7(b), 7(d) and 7(f)]. These results demonstrate that pseudospin-locked unidirectional propagations can

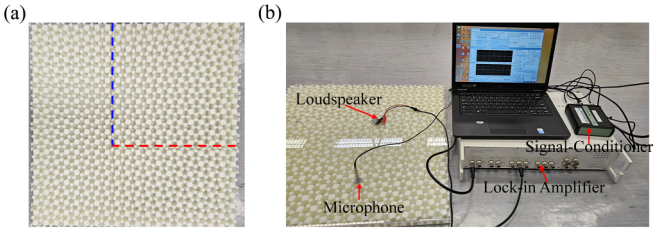

FIG. 9. Photograph of the 3D-printed experimental sample, where the vertical and horizontal interfaces are marked by the blue and red dashed lines, respectively. (b) Snapshot of the experimental setup for measuring the acoustic response.

be achieved for both the sonic modes and dual-polarization electromagnetic modes in the designed PTI.

The propagations of the helical edge mode are robust against bends. To demonstrate this, we build a waveguide structure consisting of a channel with two 90-degree sharp bends formed between two domains made of UC1s and UC2s [see Fig. 6(b)]. A point source at the left end of the channel is used to launch acoustic or electromagnetic waves. The excitation frequency for the sonic mode, TE mode, and TM mode is set as $\Omega_s = 1.1386$, $\Omega_p = 1.08$, and $\Omega_p = 0.7793$, respectively. Figures 8(a)–8(c) show the field distributions for the sonic mode, TE mode, and TM mode excited by the point source, respectively. From the figures, we can observe that waves of sonic and electromagnetic modes can all pass through the two 90-degree sharp bends in the waveguiding channel successfully, demonstrating the robustness of these edge states for all the sonic, TE and TM modes in the designed PTI.

Finally, we experimentally validate the edge states for the sonic modes while leaving the verification of the photonic modes for future works. As the dielectric materials act as hard sound boundaries for acoustic waves in the designed PTI, we use photosensitive resin, which plays the same role as silicon, for the ease of fabrication. We manufacture an experimental sample via 3D printing, as shown in Fig. 9(a), which consists of 6×6 UC1s surrounded by four layers of UC2s with the size and height of the unit cell being 60mm and 20mm, respectively. In the sample, two orthogonal interfaces are formed between the two domains made of UC1s and UC2s, indicated by the blue and red dashed lines in Fig. 9(a), respectively. To facilitate the two-dimensional waveguide assessments, an acrylic layer is

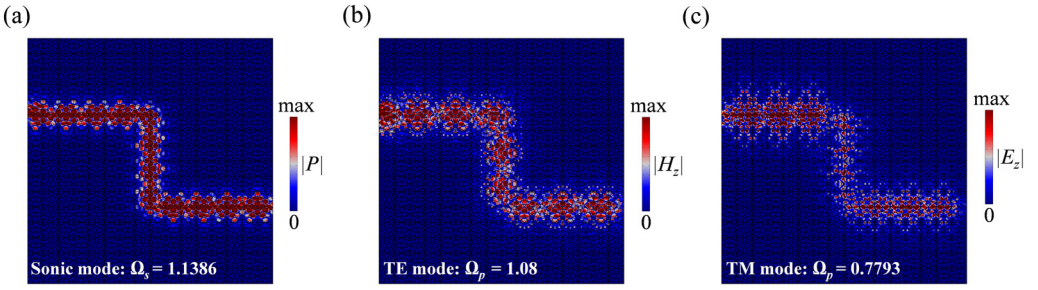

FIG. 8. Field distributions of waves passing through the bend channel for the (a) sonic mode, (b) TE mode, and (c) TM mode. The waves are launched from the left end of the channel by a source indicated by the red star shown in Fig. 6(b).

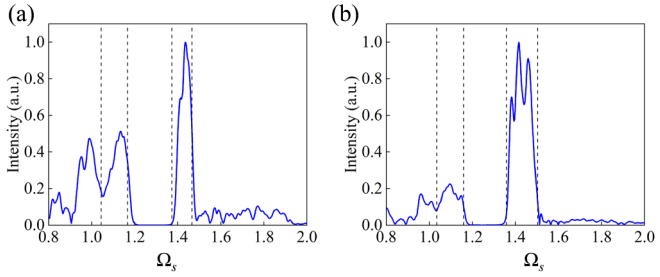

FIG. 10. Experimentally measured acoustic transmission spectrum for the (a) vertical and (b) horizontal interface, respectively. The two frequency windows indicated by the dashed lines correspond to the frequency ranges of the two pairs of helical edge states of the sonic modes in Figs. 4(a) and 4(d).

affixed atop, featuring three strategically placed apertures. These openings, typically sealed when not in use, allow for the insertion of either acoustic detection or emission devices as needed. Figure 9(b) illustrates the configuration of the experimental testing apparatus. A lock-in amplifier (Zurich Instrument HF2LI) serves dual purposes: it generates signals and also handles data acquisition. A loudspeaker, which is linked to the lock-in amplifier, is strategically placed at the intersection of the two orthogonal interfaces, whose role is to produce acoustic waves to excite the edge states. To capture the acoustic response, a 1/4-inch microphone (Brüel & Kjaer, Type 4935) is positioned within a designated hole that locates at either the horizontal or the vertical interface. The detected signal is then conveyed to the lock-in amplifier through a signal-conditional (Brüel & Kjaer, 64 NEXUS Type 2693A).

The experimentally measured acoustic transmission spectra for the two orthogonal interfaces are presented in Figs. 10(a) and 10(b), respectively. From the results, we can see that within the theoretically calculated frequency windows indicated by the dashed lines, which correspond to the frequency ranges of the two pairs of helical edge states of the sonic modes as shown in Figs. 4(a) and 4(d), enhanced acoustic responses can be observed (the tiny discrepancies mainly come from the fabrication errors). We would like to note that as part of the first pair of helical edge modes are imbedded within the bulk states, the measured responses within the lower frequency window are weaker than those corresponding to the second pair of edge modes. Nonetheless, the experiment measurements overall match well with the theoretical results presented in Figs. 4(a) and 4(d).

III. CONCLUSIONS

In conclusion, we have designed a PTI that hosts gapless helical edge states for sonic, TE, and TM photonic modes simultaneously. Using the inverse design method based on topology optimization, a glide-symmetric phoxonic crystal that hosts sonic and dual-polarization photonic bandgaps is designed first. Then by selecting two distinct unit cells from the optimized phoxonic crystal and assembling them to build a supercell with a domain-wall interface, the PTI that hosts two pairs of gapless helical edge modes of sonic, TE and TM photonic modes is created. One-way transmissions of the edge modes locked by pseudospin are demonstrated for waves of both sonic and electromagnetic modes in the same PTI waveguide structure. Moreover, the robustness of acoustic and photonic edge states is exhibited and experimental validation of the sonic edge modes is also conducted. Our work suggests a new approach to construct PTIs, having promising potentials for applications in designing topological photoacoustic devices.

ACKNOWLEDGMENTS

This work is supported by National Natural Science Foundation of China (No. 12102134), the Natural Science Foundation of Hunan Province (2022JJ40026) and the Research Grants Council of Hong Kong SAR (Grants No. 15200922 and No. 15202820).

APPENDIX: TOPOLOGY OPTIMIZATION METHOD

Ph oxonic crystals have the capabilities for controlling acoustic and electromagnetic waves simultaneously. For controlling acoustic waves, the governing equation is

$$-\nabla\cdot\left(\frac{1}{\rho(\mathbf{r})}\nabla p(\mathbf{r},\mathbf{k})\right)+\frac{1}{B(\mathbf{r})}\frac{\partial^2 p(\mathbf{r},\mathbf{k})}{\partial t^2}=0, \tag{A1}$$

in which $p(\mathbf{r},\mathbf{k})$, $\mathbf{r}(x,y)$, $\mathbf{k}=(k_x,k_y)$ are the acoustic pressure field, position vector and Bloch wave vector, respectively. $\rho(\mathbf{r})=\rho(\mathbf{r}+\mathbf{R})$ and $B(\mathbf{r})=B(\mathbf{r}+\mathbf{R})$ represent the density and bulk modulus with $\mathbf{R}$ denoting the lattice translation vector. For manipulating electromagnetic waves, which can be decoupled into TM and TE modes in two-dimensional photonic crystals [39], for which the governing equations are

$$TM:-\nabla\cdot(\nabla E_z(\mathbf{r},\mathbf{k}))+\varepsilon(\mathbf{r})\frac{\partial^2 E_z(\mathbf{r},\mathbf{k})}{\partial t^2}=0 \tag{A2}$$

$$TE:-\nabla\cdot\left(\nabla\frac{1}{\varepsilon(\mathbf{r})}H_z(\mathbf{r},\mathbf{k})\right)+\frac{\partial^2 H_z(\mathbf{r},\mathbf{k})}{\partial t^2}=0, \tag{A3}$$

where $E_z(\mathbf{r},\mathbf{k})$ and $H_z(\mathbf{r},\mathbf{k})$ represent the electric and magnetic fields, respectively. $\varepsilon(\mathbf{r})=\varepsilon(\mathbf{r}+\mathbf{R})$ means the dielectric constant. According to the Floquet-Bloch theorem, the acoustic, electric and magnetic fields, $p(\mathbf{r},\mathbf{k})$, $E_z(\mathbf{r},\mathbf{k})$, $H_z(\mathbf{r},\mathbf{k})$, can be formulated as $p(\mathbf{r},\mathbf{k})=p_{\mathbf{k}}(\mathbf{r})e^{i(\omega t+\mathbf{k}\cdot\mathbf{r})}$, $E_z(\mathbf{r},\mathbf{k})=E_{z,\mathbf{k}}(\mathbf{r})e^{i(\omega t+\mathbf{k}\cdot\mathbf{r})}$, $H_z(\mathbf{r},\mathbf{k})=H_{z,\mathbf{k}}(\mathbf{r})e^{i(\omega t+\mathbf{k}\cdot\mathbf{r})}$, respectively, where $p_{\mathbf{k}}(\mathbf{r})$, $E_{z,\mathbf{k}}(\mathbf{r})$ and $H_{z,\mathbf{k}}(\mathbf{r})$ denote the periodic functions for acoustic, electric and magnetic fields, respectively; ω denotes the angular frequency. Taking them into Eqs. (A1)–(A3) and exploiting the finite element method, Eqs. (A1)–(A3) can be written as

$$(\mathbf{K}-\omega^2\mathbf{M})\mathbf{U}=0, \tag{A4}$$

in which $\mathbf{U}$ represents the eigenvector, while $\mathbf{K}$ and $\mathbf{M}$ represent the global stiffness and mass matrices, respectively. The detailed expressions of $\mathbf{K}$ and $\mathbf{M}$ for the sonic, TE and TM modes can be referred to Ref. [39]. Via sweeping the wave vectors along the boundary of the first Brillouin zone, we can get the band diagram for the optimization design.

We denote the relative size of the n^{th}-order bandgap for the sonic modes, TE modes and TM modes as g_n^s, g_n^{TE} and g_n^{TM}, respectively, which should be maximized simultaneously. For

succinctness, g_n^s, g_n^{TE} and g_n^{TM} are collectively named g_n herein, expressed by

$$g_n = 2\frac{\min_{i=1,2\cdots L,n_k}\omega_{n+1}(\mathbf{k}_i) - \max_{i=1,2\cdots L,n_k}\omega_n(\mathbf{k}_i)}{\min_{i=1,2\cdots L,n_k}\omega_{n+1}(\mathbf{k}_i) + \max_{i=1,2\cdots L,n_k}\omega_n(\mathbf{k}_i)}, \tag{A5}$$

where n_k represents the count of wave vectors used in the computation of the band diagram. g_n is further modified using the strategy proposed in Ref. [39] to avoid numerical instabilities. According to Eq. (A5), we can get the gradient of objective function g_n, $\frac{\partial g_n}{\partial x_e}$, upon getting $\frac{\partial \omega_n(\mathbf{k}_i)}{\partial x_e}$, which can be obtained via differentiating both sides of Eq. (A1),

$$\frac{\partial \omega_n(\mathbf{k}_i)}{\partial x_e} = \frac{1}{2\omega_n}\mathbf{u}^T\left(\frac{\partial \mathbf{K}}{\partial x_e} - \omega_n^2(\mathbf{k}_i)\frac{\partial \mathbf{M}}{\partial x_e}\right)\mathbf{u}. \tag{A6}$$

Upon getting the gradient of objective functions, we employ the BESO approach [40] to iteratively update the unit cell to maximize g_n^s, g_n^{TE} and g_n^{TM} simultaneously. Note that we first maximize g_n^s herein and then adopt the optimized structure as the initial configuration for the second-round optimization.

[1] M. Z. Hasan and C. L. Kane, *Colloquium:* Topological insulators, Rev. Mod. Phys. **82**, 3045 (2010).

[2] X.-L. Qi and S.-C. Zhang, Topological insulators and superconductors, Rev. Mod. Phys. **83**, 1057 (2011).

[3] A. B. Khanikaev and G. Shvets, Two-dimensional topological photonics, Nat. Photon. **11**, 763 (2017).

[4] T. Ozawa, H. M. Price, A. Amo, N. Goldman, M. Hafezi, L. Lu, M. C. Rechtsman, D. Schuster, J. Simon, O. Zilberberg, and I. Carusotto, Topological photonics, Rev. Mod. Phys. **91**, 015006 (2019).

[5] M. Kim, Z. Jacob, and J. Rho, Recent advances in 2D, 3D and higher-order topological photonics, Light Sci. Appl. **9**, 130 (2020).

[6] Z. Lan, M. L. N. Chen, F. Gao, S. Zhang, and W. E. I. Sha, A brief review of topological photonics in one, two, and three dimensions, Rev. Phys. **9**, 100076 (2022).

[7] G. Ma, M. Xiao, and C. T. Chan, Topological phases in acoustic and mechanical systems, Nat. Rev. Phys. **1**, 281 (2019).

[8] H. Xue, Y. Yang, and B. Zhang, Topological acoustics, Nat. Rev. Mater. **7**, 974 (2022).

[9] X. Zhang, F. Zangeneh-Nejad, Z.-G. Chen, M.-H. Lu, and J. Christensen, A second wave of topological phenomena in photonics and acoustics, Nature (London) **618**, 687 (2023).

[10] F. D. M. Haldane and S. Raghu, Possible realization of directional optical waveguides in photonic crystals with broken time-reversal symmetry, Phys. Rev. Lett. **100**, 013904 (2008).

[11] Z. Wang, Y. Chong, J. D. Joannopoulos, and M. Soljacic, Reflection-free one-way edge modes in a gyromagnetic photonic crystal, Phys. Rev. Lett. **100**, 013905 (2008).

[12] Z. Wang, Y. Chong, J. D. Joannopoulos, and M. Soljacic, Observation of unidirectional backscattering-immune topological electromagnetic states, Nature (London) **461**, 772 (2009).

[13] Z. Yang, F. Gao, X. Shi, X. Lin, Z. Gao, Y. Chong, and B. Zhang, Topological acoustics, Phys. Rev. Lett. **114**, 114301 (2015).

[14] Y. Ding, Y. Peng, Y. Zhu, X. Fan, J. Yang, B. Liang, X. Zhu, X. Wan, and J. Cheng, Experimental demonstration of acoustic Chern insulators, Phys. Rev. Lett. **122**, 014302 (2019).

[15] J.-W. Liu, F.-L. Shi, X.-T. He, G.-J. Tang, W.-J. Chen, X.-D. Chen, and J.-W. Dong, Valley photonic crystals, Adv. Phys.: X **6**, 1905546 (2021).

[16] H. Xue, Y. Yang, and B. Zhang, Topological valley photonics: Physics and device applications, Adv. Photonics Res. **2**, 2100013 (2021).

[17] J. Lu, C. Qiu, M. Ke, and Z. Liu, Valley vortex states in sonic crystals, Phys. Rev. Lett. **116**, 093901 (2016).

[18] J. Lu, C. Qiu, L. Ye, X. Fan, M. Ke, F. Zhang, and Z. Liu, Observation of topological valley transport of sound in sonic crystals, Nat. Phys. **13**, 369 (2017).

[19] L.-H. Wu and X. Hu, Scheme for achieving a topological photonic crystal by using dielectric material, Phys. Rev. Lett. **114**, 223901 (2015).

[20] Y. Yang, Y. F. Xu, T. Xu, H.-X. Wang, J.-H. Jiang, X. Hu, and Z. H. Hang, Visualization of a unidirectional electromagnetic waveguide using topological photonic crystals made of dielectric materials, Phys. Rev. Lett. **120**, 217401 (2018).

[21] Y. Chen, F. Meng, B. Jia, G. Li, and X. Huang, Inverse design of photonic topological insulators with extra-wide bandgaps, Phys. Status Solidi - Rapid Res. Lett. **13**, 1900175 (2019).

[22] C. He, X. Ni, H. Ge, X.-C. Sun, Y.-B. Chen, M.-H. Lu, X.-P. Liu, and Y.-F. Chen, Acoustic topological insulator and robust one-way sound transport, Nat. Phys. **12**, 1124 (2016).

[23] Z. Zhang, Q. Wei, Y. Cheng, T. Zhang, D. Wu, and X. Liu, Topological creation of acoustic pseudospin multipoles in a flow-free symmetry-broken metamaterial lattice, Phys. Rev. Lett. **118**, 084303 (2017).

[24] X. Zhang, H.-X. Wang, Z.-K. Lin, Y. Tian, B. Xie, M.-H. Lu, Y.-F. Chen, and J.-H. Jiang, Second-order topology and multidimensional topological transitions in sonic crystals, Nat. Phys. **15**, 582 (2019).

[25] X. Zhou, J. Tong, J. Chang, and Z. Xu, Gliding photonic topological edge waves, J. Phys. D: Appl. Phys. **56**, 475303 (2023).

[26] Y. Chen, S. An, Z. Lan, L. Fan, L. An, and Z. Su, Multiband acoustic helical interface states in inverse-designed sonic crystals with glide symmetry, Compos. Struct. **335**, 117994 (2024).

[27] X.-D. Chen, W.-M. Deng, F.-L. Shi, F.-L. Zhao, M. Chen, and J.-W. Dong, Direct observation of corner states in second-order topological photonic crystal slabs, Phys. Rev. Lett. **122**, 233902 (2019).

[28] B.-Y. Xie, G.-X. Su, H.-F. Wang, H. Su, X.-P. Shen, P. Zhan, M.-H. Lu, Z.-L. Wang, and Y.-F. Chen, Visualization of higher-order topological insulating phases in two-dimensional dielectric photonic crystals, Phys. Rev. Lett. **122**, 233903 (2019).

[29] Y. Chen, Z. Lan, and J. Zhu, Inversely designed second-order photonic topological insulator with multiband corner states, Phys. Rev. Appl. **17**, 054003 (2022).

[30] X. Zhang, L. Liu, M.-H. Lu, and Y.-F. Chen, Valley-selective topological corner states in sonic crystals, Phys. Rev. Lett. **126**, 156401 (2021).

[31] Y. Chen, X. Wen, Z. Gu, J. Zhu, and Z. Su, Customizable multiband second-order sonic topological

insulators via inverse design, Int. J. Mech. Sci. **260**, 108669 (2023).

[32] B. Xie, H.-X. Wang, X. Zhang, P. Zhan, J.-H. Jiang, M. Lu, and Y. Chen, Higher-order band topology, Nat. Rev. Phys. **3**, 520 (2021).

[33] B. Xia, H. Fan, and T. Liu, Topologically protected edge states of phoxonic crystals, Int. J. Mech. Sci. **155**, 197 (2019).

[34] Z. Hu, L. Lei, L. He, W. Liu, T. Yu, T. Wang, and Q. Liao, Simultaneous photonic and phononic topological pseudospin-dependent edge states in phoxonic crystals, Europhys. Lett. **138**, 15001 (2022).

[35] Y. Chen, Z. Lan, Z. Su, and J. Zhu, Inverse design of photonic and phononic topological insulators: A review, Nanophotonics **11**, 4347 (2022).

[36] L. Zhang, Y. Yang, Z. K. Lin, P. Qin, Q. Chen, F. Gao, E. Li, J. H. Jiang, B. Zhang, H. Chen, Higher-order topological states in surface-wave photonic crystals, Adv. Sci. **7**, 1902724 (2020).

[37] Y. Chen, Z. Lan, and J. Zhu, Second-order topological phases in C_{4v}-symmetric photonic crystals beyond the two-dimensional Su-Schrieffer-Heeger model, Nanophotonics **11**, 1345 (2022).

[38] R. Jackiw and C. Rebbi, Solitons with fermion number 1/2, Phys. Rev. D **13**, 3398 (1976).

[39] F. Meng, X. Huang, and B. Jia, Bi-directional evolutionary optimization for photonic band gap structures, J. Comput. Phys. **302**, 393 (2015).

[40] X. Huang and Y. M. Xie, *Evolutionary Topology Optimization of Continuum Structures: Methods and Applications*, (John Wiley & Sons, New Jersey, 2010).